# Supporting Information

Disorder-Driven Current Filamentation and Electro–Thermal Instability in Halide Solid Electrolytes:
A Disordered Network Model with Impedance Signatures

Dongwook Lee[1,*] Jiwon Seo[1,**]

[1]Department of Physics and Engineering Physics, Yonsei University
MIRAE Campus,
Wonju-si, Gangwon-do 26493, Republic of Korea

[*]Corresponding author: dongwookleedl324@yonsei.ac.kr
[**]Corresponding author: jiwonseo@yonsei.ac.kr

## Contents

# S1 Control model comparison

To assess the role of the pathway-suppression noise $\eta_i$ in the full model (Model A+B), three model variants are compared at $N = 15$ (8 seeds each):

- **Model A** (pure Arrhenius): $g_i = g_0 \exp(-E_{a,i}/k_B T)$ with Gaussian $E_{a,i}$ disorder only; no $\eta_i$ term. This is the *core model* used in the main text.
- **Model A+B** (full model): adds the exponential suppression factor $\exp(-\eta_i)$ as described in the main text.
- **Model C** (correlated): spatially correlated Gaussian $E_a$ field (correlation length 3 lattice units); no $\eta_i$ term.

Fig. S1 shows that Model A already produces strong filamentation with a peak near $\sigma_E \approx 0.16\,\text{eV}$, reaching $\Phi \approx 11.8$. Model A+B enhances the peak by $\approx 6\%$ without shifting its location; all main-text figures use Model A. Model C produces qualitatively different behaviour (broader, shifted peak), confirming that the peaked shape reflects uncorrelated activation-energy statistics, not a model construction artifact.

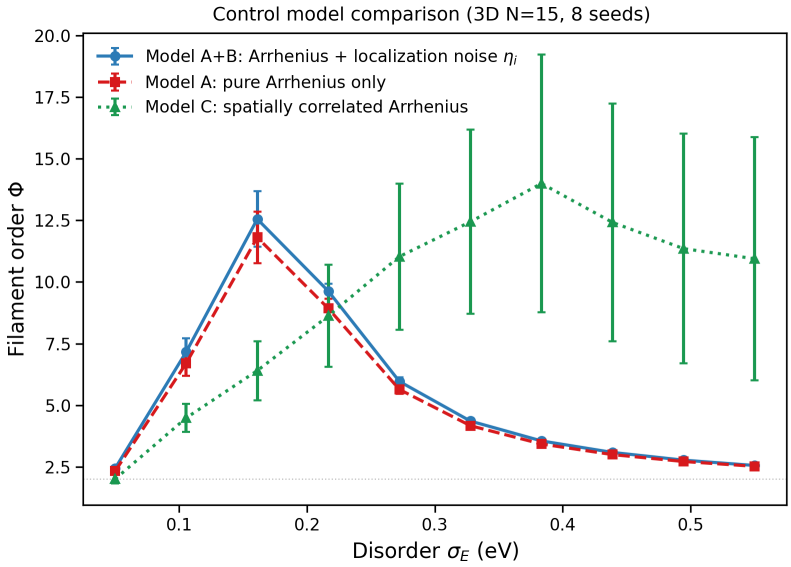


**Figure S1.** Control model comparison (3D, $N = 15$, 8 seeds each). Model A (red dashed) and Model A+B (blue solid) peak at the same $\sigma_E$ and differ by $\approx 6\%$ in amplitude. Model C (green dotted) shows qualitatively different behaviour. Error bars: 1 SE.

# S2 Ensemble AC impedance — DC and AC correlation

Fig. S2 shows AC impedance spectra and the DC–AC correlation computed from the same 3D disordered networks ($N = 15$, 15 realisations each) with $C_{ij} \propto g_{ij}^{0.3}$.

Panel S2a shows ensemble-averaged Nyquist plots for four disorder values. Panel S2b shows that the DRT proxy width peaks near $\sigma_E \approx 0.25\,\mathrm{eV}$, approximately 0.10 eV above the $\Phi$ peak ($\sigma_E \approx 0.15\,\mathrm{eV}$). At the $\Phi$ peak, current is concentrated in fast filaments with relatively uniform RC time constants; the DRT broadens maximally at slightly higher disorder when the resistance landscape is most heterogeneous. Panel S2c shows the $\Phi$–DRT scatter (Pearson $r = 0.71$), confirming a moderate positive correlation.

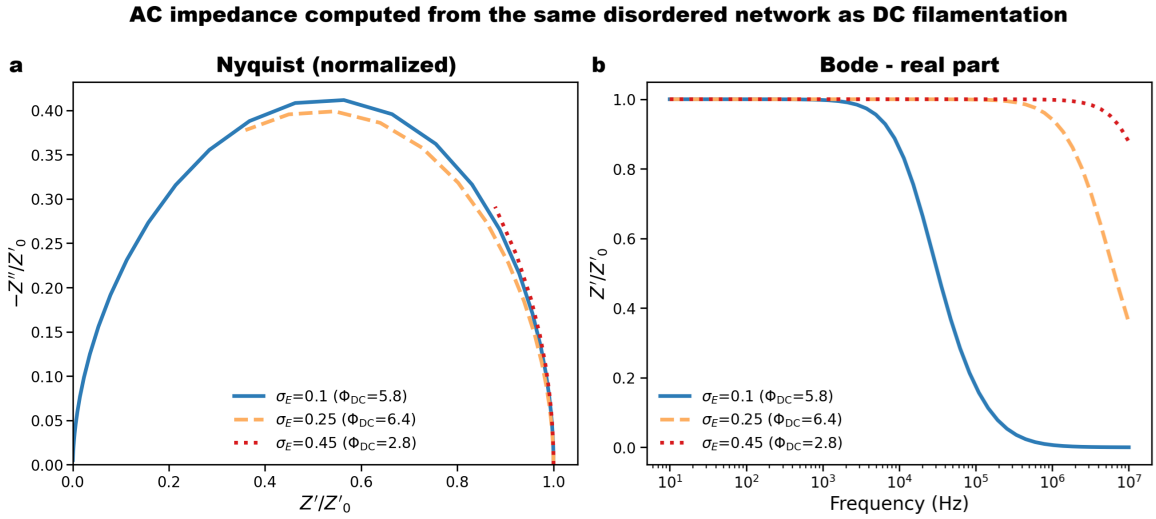


**Figure S2.** Ensemble AC impedance ($N = 15$, 15 seeds). (a) Ensemble-averaged Nyquist plots. (b) DRT proxy width vs $\sigma_E$. (c) $\Phi$ vs DRT width scatter; Pearson $r = 0.71$.

Extended calculations at $N = 20$ and $N = 25$ (5 seeds each) are shown in Fig. S6; the key result is that the non-monotonic DRT broadening trend is preserved across all three system sizes.

# S3 High-resolution $\sigma_E$ scan near peak

The coarse FSS grid ($\Delta\sigma_E \approx 0.045\,\mathrm{eV}$) places the peak at the second of twelve sampled values. To verify this is a genuine interior maximum, a dedicated high-resolution scan was performed over $\sigma_E = 0.08$–$0.26\,\mathrm{eV}$ with $\Delta\sigma_E \approx 0.018\,\mathrm{eV}$ (15 points), at $N = 40$ with 20 seeds each.

Fig. S3 shows the result. The refined peak is at $\sigma_E = 0.170\,\mathrm{eV}$ ($\Phi = 11.26 \pm 0.15$), clearly interior to the scanned range with both flanks well resolved. The coarse-grid data agree with the high-resolution scan where they overlap. No boundary artifact is present.

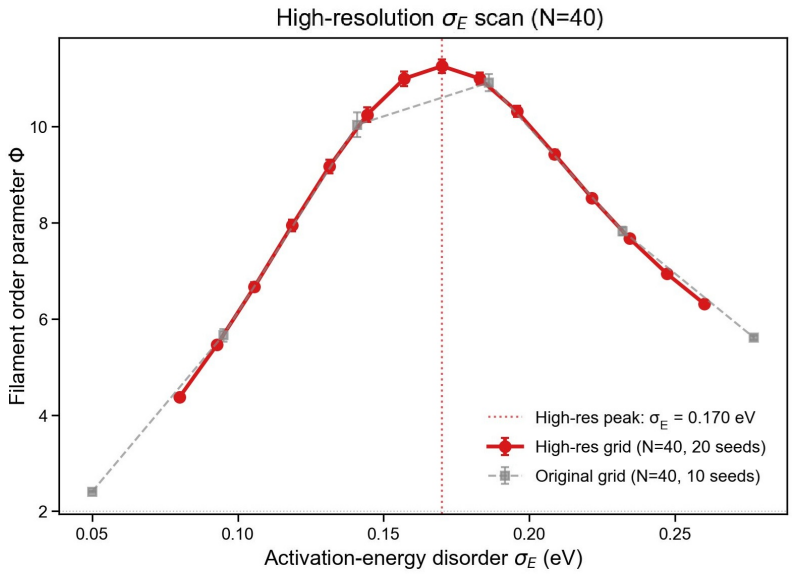


**Figure S3.** High-resolution $\sigma_E$ scan ($N = 40$, 20 seeds, red circles). Coarse grid ($N = 40$, 10 seeds, grey squares) shown for comparison. Refined peak at $\sigma_E = 0.170\,\mathrm{eV}$ ($\Phi = 11.26$). Error bars: 1 SE.

# S4 Finite-size scaling — fit form comparison

The main text uses $\Phi(N) = \Phi_\infty + A/N$. Fig. S4 compares three fit forms on peak $\Phi$ data for $N = 20$–$60$ (6 points, weighted by inverse SE):

- **Form 1** (linear $1/N$): $\Phi(N) = \Phi_\infty + A/N$. Direct fit: $\Phi_\infty = 10.64 \pm 0.16$; bootstrap: $\Phi_\infty = 10.52 \pm 0.20$ (used in main text). AIC = 7.9.
- **Form 2** (power law): $\Phi(N) = \Phi_\infty + A/N^\omega$. $\Phi_\infty = 10.82 \pm 0.31$, $\omega = 1.85$, AIC = 8.9. Additional parameter not justified by AIC.
- **Form 3** (quadratic): $\Phi(N) = \Phi_\infty + A/N + B/N^2$. $\Phi_\infty = 11.45 \pm 0.55$, AIC = 7.5. Larger uncertainty reflects overfitting with 6 data points.

All three forms yield $\Phi_\infty = 10.6$–$11.5$, consistent within quoted uncertainties. The linear form is the most parsimonious and is used in the main text.

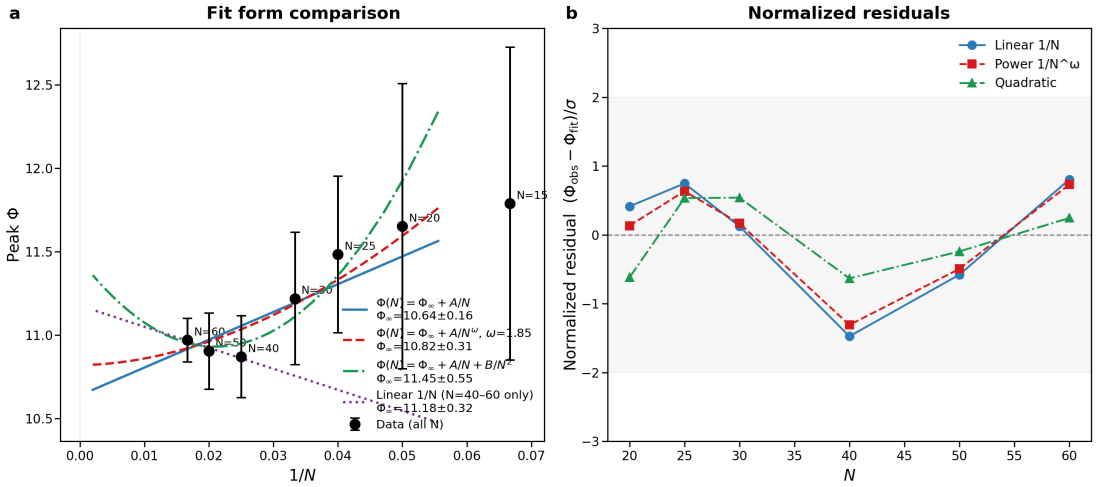


**Figure S4.** FSS fit form comparison. (a) Peak $\Phi$ vs $1/N$ for $N = 20$–$60$; linear (blue), power-law (red dashed), quadratic (green) fits. Star: $\Phi_\infty = 10.52 \pm 0.20$. (b) Normalised residuals.

# S5 3D instability boundary: $N = 25$, 40, 50 comparison

Fig. S5 documents the finite-size dependence of the 3D $V_{\mathrm{crit}}$ boundary.

Panel S5a shows $V_{\mathrm{crit}}(\sigma_E)$ for $N = 25$ (10 seeds), $N = 40$ (6 seeds), and $N = 50$ (4 seeds). The instability onset $\sigma_E \approx 0.22\,\mathrm{eV}$ is identical for all three sizes, confirming robustness. The $V_{\mathrm{crit}}$ plateau increases monotonically: 1.17 V ($N = 25$), 1.46 V ($N = 40$), 1.75 V ($N = 50$).

Panel S5b shows the plateau $V_{\mathrm{crit}}$ vs $1/N$; a linear fit ($R^2 = 0.92$) extrapolates to a model-defined threshold of ∼2.2 V. This is a dimensionless network voltage and is not directly comparable to a full cell voltage; its practical interpretation requires calibration of the local electrolyte potential drop for specific cell geometries.

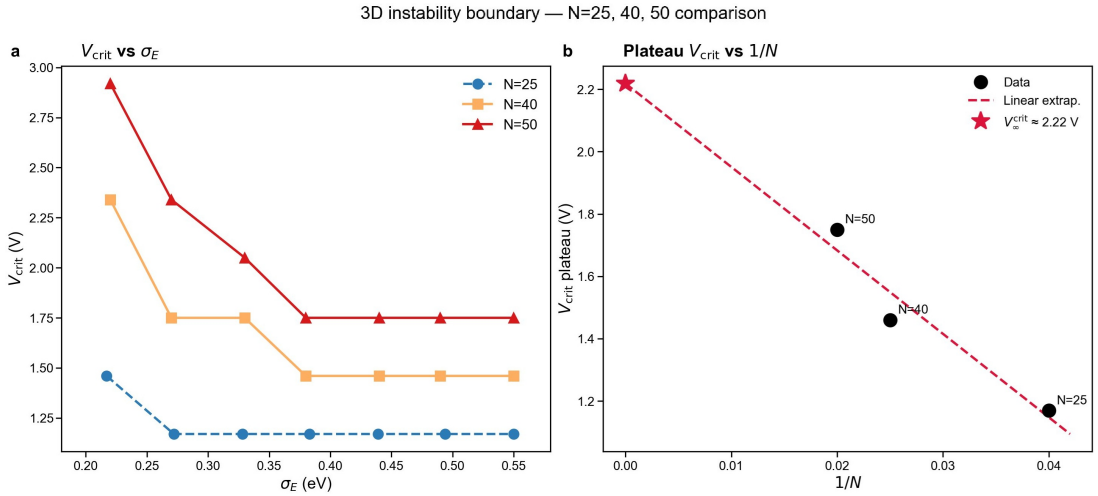


**Figure S5.** 3D $V_{\mathrm{crit}}$ finite-size comparison. (a) $V_{\mathrm{crit}}$ vs $\sigma_E$ for $N = 25$, 40, and 50. Onset disorder (0.22 eV) identical across sizes. (b) Plateau $V_{\mathrm{crit}}$ vs $1/N$; model threshold ∼2.2 V ($R^2 = 0.92$; network voltage, not full cell voltage).

## Extended impedance analysis: $N = 15$, 20, 25 comparison

Fig. S6 extends the DC–AC analysis from Section S2 to $N = 20$ and $N = 25$ (5 seeds each). The DRT width non-monotonic trend—rising then falling with $\sigma_E$—is preserved across all three system sizes (Fig. S6a), confirming it is not a finite-size artifact. The Pearson correlation decreases modestly with $N$: $r = 0.71$ ($N = 15$), 0.68 ($N = 20$), 0.61 ($N = 25$). This decrease is expected because $\Phi$ grows substantially with $N$ while the DRT width variation ($\sim 0.4$ decades) remains moderate; the 5-seed ensembles for larger sizes carry greater statistical uncertainty. The qualitative conclusion—a moderate positive correlation between DC filamentation and AC DRT broadening—is consistent across all sizes.

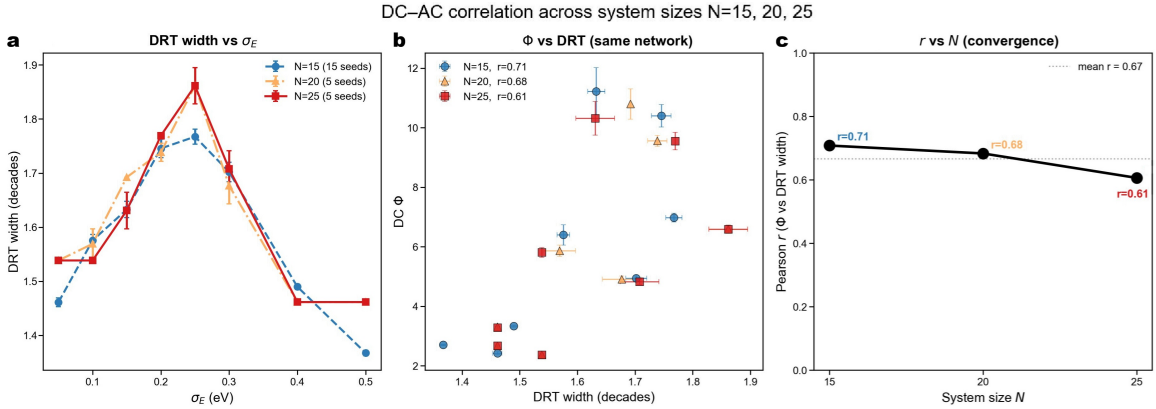


**Figure S6.** DC–AC correlation across system sizes $N = 15, 20, 25$. (a) DRT width vs $\sigma_E$; non-monotonic peak preserved. (b) $\Phi$ vs DRT scatter; Pearson $r$ decreases from 0.71 to 0.61 with increasing $N$, reflecting growth of the $\Phi$ range. (c) $r$ vs $N$. $N = 20, 25$: 5 seeds; $N = 15$: 15 seeds.

# S6 Thermal criterion: physical parameter table

Table S1 provides the physical parameter estimates used to convert dimensionless network power $Q_i$ to the normalised instability criterion $\theta_i = Q_i/Q_{\mathrm{crit}}$.

The thermal conductance per node is estimated as:

$$G_{\mathrm{th}} \sim \frac{k_{\mathrm{th}}\, A_{\mathrm{node}}}{\ell} = k_{\mathrm{th}}\, \frac{L}{N}, \tag{S1}$$

where $\ell = L/N$ is the node length and $A_{\mathrm{node}} = \ell^2$. Note the conductance scales as $k_{\mathrm{th}}L/N$ (not $k_{\mathrm{th}}N/L$) because a larger node presents a larger cross-section. This expression is used only to set an order-of-magnitude threshold.

It is emphasised that $Q_{\mathrm{crit}}$ is a calibration parameter within the dimensionless network, not derived from first principles; its sensitivity is verified over a factor-of-three range.

**Table S1.** Physical parameters for the thermal criterion.

| Quantity | Symbol | Value | Unit | Source |
|---|---|---|---|---|
| Electrolyte thickness | $L$ | 100 | $\mu$m | Typical dense pellet |
| Thermal conductivity | $k_{\mathrm{th}}$ | 0.5–1.5 | $\mathrm{W\,m^{-1}\,K^{-1}}$ | Lit. halides [1, 2] |
| Allowable $\Delta T$ | $\Delta T_{\mathrm{max}}$ | 30–100 | K | Degradation onset [3] |
| Ionic conductivity | $\sigma_{\mathrm{ion}}$ | 0.1–1.0 | $\mathrm{mS\,cm^{-1}}$ | Lit. halides |
| Applied field | $E = V/L$ | 3–35 | $\mathrm{kV\,m^{-1}}$ (= 3–35 $\mathrm{V\,mm^{-1}}$) | $V$ = 0.3–3.5 V across $L = 100\,\mu$m |
| Current density | $J = \sigma_{\mathrm{ion}}E$ | 3–350 | $\mathrm{mA\,cm^{-2}}$ | Derived |
| Volumetric dissipation | $q = J^2/\sigma_{\mathrm{ion}}$ | $10^5$–$10^8$ | $\mathrm{W\,m^{-3}}$ | Derived |
| Normalised threshold | $\theta = 1$ level | $2\text{–}5 \times 10^{-3}$ | (dim.less) | Order-of-magnitude |
| Value used | $Q_{\mathrm{crit}}$ | $2.97 \times 10^{-3}$ | (dim.less) | Within estimated range |

The sensitivity of the phase-diagram topology to $Q_{\mathrm{crit}}$ was tested over a factor-of-three range ($1\text{–}6 \times 10^{-3}$). The qualitative structure—three regimes, monotonic decrease of $V_{\mathrm{crit}}$ with $\sigma_E$, and the plateau—is unchanged. The absolute $V_{\mathrm{crit}}$ shifts by $\approx \pm 20\%$ over this range.

# S7 Capacitance exponent sensitivity

The assignment $C_{ij} \propto g_{ij}^{\alpha}$ is phenomenological; $\alpha = 0.3$ was chosen as a mild correlation value. Fig. S7 compares the DRT proxy width vs $\sigma_E$ for $\alpha = 0$, 0.3, 0.5, 1.0 (all at $N = 8$, 4 seeds).

Fig. S7a shows that the absolute DRT width and peak location shift with $\alpha$ at small system size. Fig. S7b shows the same data normalised to each curve's peak. The non-monotonic shape is preserved for $\alpha = 0$, 0.3, and 0.5; the qualitative trend is therefore a property of the network's disorder structure, not an artifact of the capacitance parameterisation. For $\alpha = 1.0$ the trend flattens at larger disorder, motivating the choice $\alpha = 0.3$ in the main text.

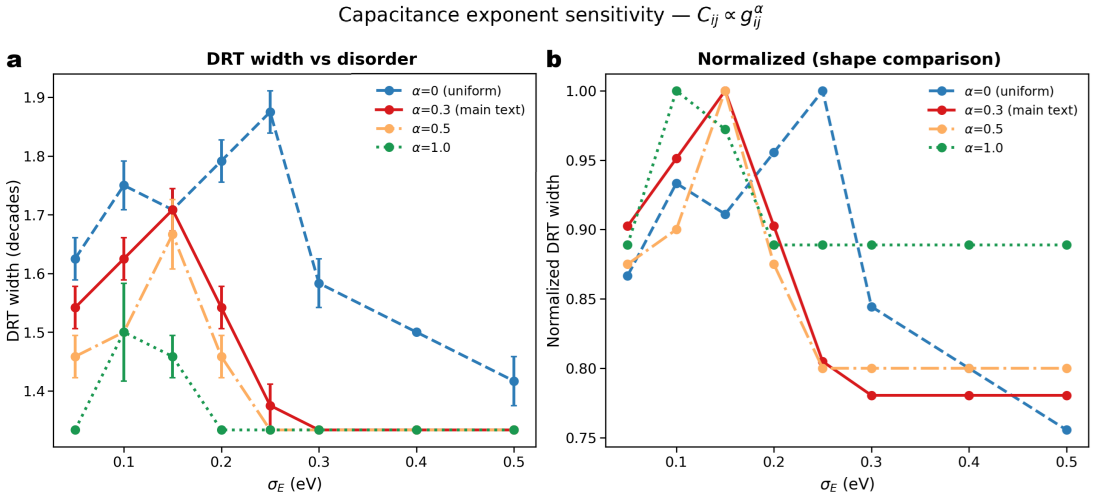


**Figure S7.** Capacitance exponent sensitivity ($C_{ij} \propto g_{ij}^{\alpha}$, $N = 8$, 4 seeds). (a) DRT width vs $\sigma_E$ for $\alpha = 0$, 0.3, 0.5, 1.0. (b) Normalised data; non-monotonic broadening preserved for $\alpha \leq 0.5$.

# S8 Model parameter summary

**Table S2.** Summary of model parameters.

| Parameter | Symbol | Value | Notes |
|---|---|---|---|
| Mean activation energy | $\bar{E}_a$ | 0.30 eV | Representative halide |
| Temperature | $T$ | 300 K | Room temperature |
| Percolation threshold | $\sigma_c$ | 0.70 eV | Model parameter |
| Correlation exponent (3D) | $\nu$ | 0.88 | 3D percolation universality |
| Correlation exponent (2D) | $\nu$ | 1.00 | 2D percolation universality |
| 3D system sizes (FSS) | $N$ | 15,20,25,30,40,50,60 | $N^3$ nodes each |
| Seeds per point (FSS) | $n_s$ | 20 | SE $< 5\%$ |
| 2D system sizes | $N$ | up to 100 | $N^2$ nodes |
| Phase diagram seeds (3D) | $n_s$ | 4–10 | $N = 25$: 10; $N = 40$: 6; $N = 50$: 4 |
| Instability threshold | $Q_{\text{crit}}$ | $2.97 \times 10^{-3}$ | See Table S1 |
| Capacitance exponent | $\alpha$ | 0.3 | Phenomenological; see Fig. S7 |

# S9 Disorder distribution sensitivity

The main text uses a Gaussian activation-energy disorder distribution, which is the standard choice for thermally activated hopping in disordered solids. Fig. S8 compares $\Phi(\sigma_E)$ for four distributions at $N = 15$ (5 seeds each), all with the same mean $\bar{E}_a = 0.30\,\text{eV}$ and the same standard deviation $\sigma_E$: Gaussian (main text), exponential (one-sided, heavier tail), uniform ($\pm\sqrt{3}\sigma_E$ range), and bimodal (two Gaussians centred at $E_a = \bar{E}_a \pm \sigma_E$, each with width $\sigma_E/2$).

Fig. S8a shows that the peak amplitude and location depend on the distribution choice: the exponential distribution shifts the peak to $\sigma_E \approx 0.30\,\text{eV}$ with lower amplitude (Pearson $r$ between tail weight and peak shift); the uniform distribution gives an intermediate peak at $\sigma_E \approx 0.20\,\text{eV}$; the bimodal distribution yields a sharp peak at $\sigma_E \approx 0.15\,\text{eV}$. Fig. S8b shows the same data normalised to each curve's peak value. The key observation is that the non-monotonic topology—$\Phi$ rises then falls with $\sigma_E$—is preserved for all four distributions. The Gaussian choice is therefore not anomalous; the qualitative conclusion is generic across disorder distribution families.

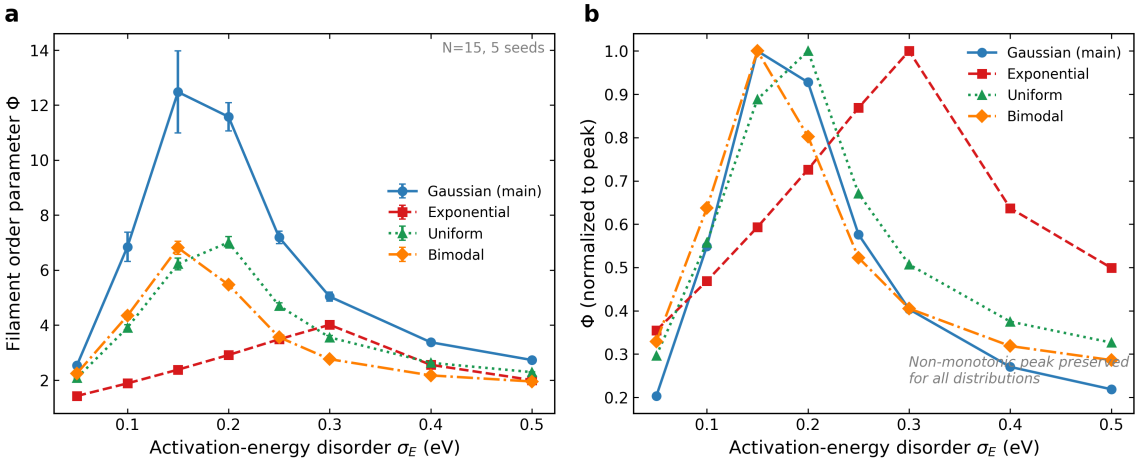


**Figure S8.** Disorder distribution sensitivity ($N = 15$, 5 seeds each). (a) $\Phi(\sigma_E)$ for Gaussian (main text), exponential, uniform, and bimodal activation-energy distributions. Peak position and amplitude shift with distribution choice, but the non-monotonic topology is preserved in all cases. (b) Same data normalised to each curve's peak, confirming the qualitative robustness of the filamentation mechanism.

# References


[1] J. Janek, W. G. Zeier, A solid future for battery development, *Nat. Energy* **1** (2016) 16141.

[2] T. Famprikis, P. Canepa, J. A. Dawson, M. S. Islam, C. Masquelier, Fundamentals of inorganic solid-state electrolytes for batteries, *Nat. Mater.* **18** (2019) 1278–1291.

[3] Z. Song, T. Wang, H. Yang, W. H. Kan, Y. Chen, Q. Yu, L. Wang, Y. Zhang, Y. Dai, H. Chen, W. Yin, T. Honda, M. Avdeev, H. Xu, J. Ma, Y. Huang, W. Luo, Promoting high-voltage stability through local lattice distortion of halide solid electrolytes, *Nat. Commun.* **15** (2024) 1481.

[4] M. Saccoccio, T. H. Wan, C. Chen, F. Ciucci, Optimal regularization in distribution of relaxation times applied to electrochemical impedance spectroscopy: ridge and lasso regression methods – a theoretical and experimental study, *Electrochim. Acta* **147** (2014) 470–482.

[5] T. H. Wan, M. Saccoccio, C. Chen, F. Ciucci, Influence of the discretization methods on the distribution of relaxation times deconvolution: implementing radial basis functions with DRTtools, *Electrochim. Acta* **184** (2015) 483–499.